High harmonic generation in solids: Real versus virtual transition channels

A. Thorpe ⬤,[1,*,‡] N. Boroumand ⬤,[1,†,‡] A. M. Parks,[1] E. Goulielmakis ⬤,[2] and T. Brabec[1]
[1]Department of Physics, University of Ottawa, Ottawa, Ontario, Canada K1N 6N5
[2]Institute of Physics, University of Rostock, Rostock D-18059, Germany

A closed-form formalism for modeling high harmonic generation (HHG) in solids is derived; its validity is tested for one-dimensional two-band inversion symmetric model solids; excellent agreement with the exact von Neumann equation is found. From the closed-form expressions, a diagnostic method is developed that allows one to separate resonant from nonresonant processes in nonlinear optics. This opens a deeper view into the dominant laser- and material-dependent mechanisms of high harmonic generation in solids. Midinfrared-driven HHG in semiconductors is dominated by the resonant interband current. As a result of the dynamic Stark shift, virtual processes gain in importance in near-infrared-driven HHG in dielectrics. Finally, comparison to experiments indicates the potential importance of little-explored processes, such as dephasing of the strong-field dynamics from coupling to the many-body environment of solids.

I. INTRODUCTION

Since its first demonstration a decade ago [1], high harmonic generation (HHG) in solids has opened novel avenues to probe material properties, such as the crystal momentum-dependent band gap [2–6], Berry phase [7,8], and valence potential [9]; further, the sensitivity of HHG to lattice asymmetry [10], to topological properties, and correlation of materials [11–21] has been explored.

HHG research can be distinguished by material and laser wavelength: semiconductors exposed to (i) far-infrared (far-ir) [6,22–24] and (ii) mid-ir [1,25–31] lasers, and (iii) dielectrics driven by near-ir lasers [3,4,9].

Quantitative numerical modeling of HHG experiments in solids is challenging, and it is even more challenging to extract insight into physical mechanisms from numerical analysis. Therefore, there is still considerable uncertainty about the various dominant mechanisms in the three experimental settings, impeding further development of HHG technology. The prevalent assumption is that HHG is driven by real (resonant) transitions. Simple model analysis suggests the following picture. Laser-induced electron-hole pair creation is followed by HHG via interband polarization buildup in (ii) [25,27,32–37] or via the intraband nonlinearity of individual bands in (iii) [3,4]. Why different mechanisms dominate different experimental setups remains a central, open question.

The contribution of virtual (nonresonant) nonlinear processes to HHG in solids, and to extreme nonlinear optics (NLO) in general, has been disregarded so far, despite their ubiquitous importance in perturbative NLO [38]. Recent mid-ir semiconductor HHG experiments have indicated the importance of virtual processes for below minimum band-gap harmonics [39]; further, light field control of real and virtual carriers has recently been demonstrated [40]. As such, the role of resonant versus virtual processes needs to be clarified for a more complete understanding of extreme nonlinear optics in general and for HHG in particular. Real (resonant) and virtual (nonresonant) transitions are depicted in the schematic in Fig. 1(a). While resonant and virtual processes can be separated in perturbative NLO, this has not been possible in extreme NLO to date and presents uncharted territory; see the schematic in Fig. 1(b).

Here, closed-form expressions for resonant and virtual nonlinear processes are obtained that are valid from the perturbative to the extreme realms of NLO, thus allowing a unified description of resonant and virtual NLO.

Our approach builds on the adiabatic following approach [38] of perturbative NLO, which accounts only for virtual transitions in under-resonant laser fields. In the intense field limit, virtual and real transitions become relevant, which are both captured by the strong-field adiabatic following (SFAF) approach. This is achieved by an exact solution of the von Neumann equation for an electron-hole pair, followed by an expansion into a Dyson series. The zero-order contribution reproduces the conventional adiabatic following approach. The first- and second-order expansion terms thus yield closed-form equations for real and virtual interband and intraband currents, allowing a more fine-grained characterization of mechanisms driving HHG in solids. The validity of the SFAF method is tested using one-dimensional (1D), two-band models for semiconductors and dielectrics. Excellent agreement between the exact von Neumann and the SFAF equations is found. By contrast, another commonly used approximation, the frozen valence band (FVB) approach [41], is found to work well for mid-ir-driven semiconductors, but fails for near-ir-driven dielectrics due to the increasing importance of the dynamic Stark shift.

*athor087@uottawa.ca
†nboro046@uottawa.ca
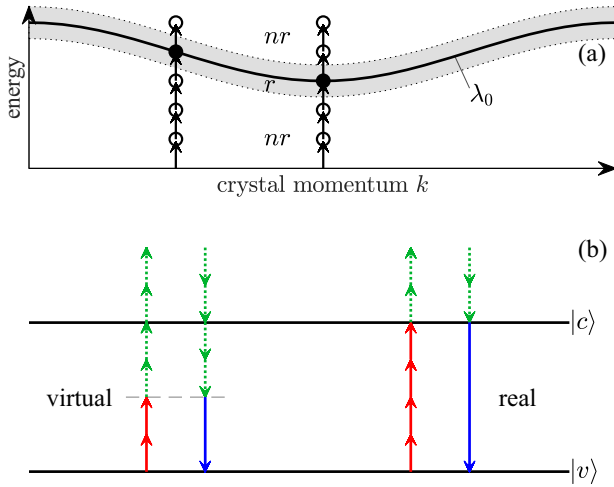‡These authors contributed equally to this work.

FIG. 1. (a) Real (resonant) vs virtual (nonresonant) processes. Real transitions (full circles) happen at crystal momenta k for which the laser dressed band gap λ_0 (full line) is bridged by n photons, ensuring energy conservation. Virtual transitions (empty circles) do not fulfill energy conservation and return to the ground state after the laser pulse. For finite laser pulses, photon energies are slightly varying, blurring the sharp transition requirement (shaded area). (b) Perturbative vs strong-field NLO; in perturbative NLO, only the lowest-order absorption channel (full arrows up) dominates, making virtual (left) and real (right) transitions readily distinguishable. In intense fields, a large number of higher-order, net-zero-photon processes (dashed arrows) become important, complicating the separation.

The SFAF approach is applied to analyzing (ii) mid-ir semiconductor and (iii) near-ir dielectric HHG. We identify the dominant mechanisms driving HHG in the two experimental settings and make progress in understanding the source of their different behavior. The results for (ii) agree with and expand on previous findings. Resonant/nonresonant interband HHG dominate above/below the band gap, and intraband HHG is negligible. In the near-ir dielectric model system (iii), real and virtual HHG channels become more comparable, as real transitions are weakened due to a more pronounced role of the dynamic Stark shift. Beyond that, comparison of our results to experiments in (iii) indicates the potential importance of additional processes, such as dephasing of the strong-field dynamics in the many-body condensed-matter environment. This charts the way towards a more complete understanding of the physical mechanisms driving HHG in solids.

II. STRONG-FIELD ADIABATIC FOLLOWING FORMALISM

Our analysis starts from the von Neumann (one-body semiconductor Bloch) equation for density matrix ρ,

$$i\partial_t \rho(\mathbf{K}, t) = [H(\mathbf{K}_t, t), \rho(\mathbf{K}, t)], \tag{1}$$

derived in the moving crystal momentum frame $\mathbf{K}_t = \mathbf{K} + \mathbf{A}(t)$, with crystal momentum $\mathbf{K}$ defined in the shifted first Brillouin zone, $\overline{\mathrm{BZ}} = \mathrm{BZ} - \mathbf{A}(t)$. The vector potential is $\mathbf{A}(t)$ and the electric field $\mathbf{F}(t) = -\partial_t \mathbf{A}(t)$. Electron-hole interaction is neglected. We use atomic units, unless specified

otherwise. The Hamilton operator H is given by [42]

$$H(\mathbf{K}_t, t) = \frac{1}{2} \begin{bmatrix} \varepsilon(\mathbf{K}_t) & \Omega(\mathbf{K}_t, t) \\ \Omega(\mathbf{K}_t, t) & -\varepsilon(\mathbf{K}_t) \end{bmatrix}, \tag{2}$$

with $\Omega(\mathbf{K}_t, t) = 2\mathbf{F}(t)\mathbf{d}_{vc}(\mathbf{K}_t)$ the Rabi frequency and $\mathbf{d}_{vc}$ the transition dipole element between the valence and conduction bands. We confine our analysis to inversion symmetric materials with a purely real or imaginary transition dipole; we use the gauge freedom of the Bloch eigenfunctions to choose a real dipole, $\mathbf{d}_{vc} = \mathbf{d}_{cv} = \mathbf{d}$. The band gap $\varepsilon(\mathbf{K}) = E_c(\mathbf{K}) - E_v(\mathbf{K})$ is the difference between the conduction and valence energy bands E_c, E_v, respectively. The density operator and Hamiltonian are defined with respect to the Bloch basis functions $|v\rangle(\mathbf{K}_t), |c\rangle(\mathbf{K}_t)$, for the valence and conduction bands, respectively; e.g., H_{11} refers to basis $|c\rangle\langle c|$.

In the limit of laser frequency much smaller than the minimum band gap, the electron dynamics dominantly follows the laser field and the adiabatic following approximation can be used. This is done by first diagonalizing the Hamiltonian (2),

$$\widetilde{H}(\mathbf{K}_t, t) = V^+ H V = \frac{1}{2} \begin{bmatrix} \lambda(\mathbf{K}_t, t) & 0 \\ 0 & -\lambda(\mathbf{K}_t, t) \end{bmatrix}, \tag{3}$$

with $\lambda(\mathbf{K}_t, t) = \sqrt{\varepsilon^2(\mathbf{K}_t) + |\Omega(\mathbf{K}_t, t)|^2}$ and unitary matrix

$$V(\mathbf{K}_t, t) = \frac{1}{\sqrt{2}} \begin{bmatrix} \frac{\sqrt{\lambda + \varepsilon}}{\sqrt{\lambda}} & -\frac{\Omega}{\sqrt{\lambda}\sqrt{\lambda + \varepsilon}} \\ \frac{\Omega}{\sqrt{\lambda}\sqrt{\lambda + \varepsilon}} & \frac{\sqrt{\lambda + \varepsilon}}{\sqrt{\lambda}} \end{bmatrix}. \tag{4}$$

By multiplying the von Neumann equation with V^+, V from the left and right, inserting $VV^+ = \mathbb{1}$ and defining $\tilde{\rho} = V^+ \rho V$ yields the transformed but still exact equation

$$i\partial_t \tilde{\rho} = [\widetilde{H}, \tilde{\rho}] + i(\partial_t V^+)V\tilde{\rho} + i\tilde{\rho}V^+(\partial_t V). \tag{5}$$

The integration of Eq. (5) and transformation back to ρ yields

$$\rho(\mathbf{K}, t) = X^+(\mathbf{K}, t)\rho(\mathbf{K}, t = -\infty)X(\mathbf{K}, t),$$
$$X(\mathbf{K}, t) = \left(\hat{T}e^{\int_{-\infty}^t d\tau W(\mathbf{K}, \tau)}\right)^+ e^{i\int_{-\infty}^t d\tau \widetilde{H}(\mathbf{K}_\tau)}V^+(\mathbf{K}_t),$$
$$W(\mathbf{K}, t) = e^{i\int_{-\infty}^t d\tau \widetilde{H}(\mathbf{K}_\tau)}(\partial_t V^+(\mathbf{K}_t))V(\mathbf{K}_t)e^{-i\int_{-\infty}^t d\tau \widetilde{H}(\mathbf{K}_\tau)}. \tag{6}$$

Equation (6) is exact. For the sake of brevity, we omit the explicit time dependence in $V, V^+, \widetilde{H}, \Omega$, and λ from Eq. (6) onward. Here, $X(\mathbf{K}, t)$ and $W(\mathbf{K}, t)$ are matrix operators introduced to simplify the presentation of Eq. (6), and $\hat{T}$ refers to the time-ordering operator, which numerically is evaluated as $\hat{T}e^{\int_{-\infty}^t d\tau W(\mathbf{K}, \tau)} = \Pi_{j=0}^n e^{W(\mathbf{K}, t_j)d\tau}$ on a time window between t_0 and t_n with step size $d\tau \to 0$ small enough to converge. The time-ordered operator can be expanded into a Dyson series [43]; keeping terms up to second order yields

$$\hat{T}e^{\int_{-\infty}^t d\tau W(\mathbf{K}, \tau)} \approx 1 + \int_{-\infty}^t dt' \, W(\mathbf{K}, t') + \int_{-\infty}^t dt' \, W(\mathbf{K}, t')$$
$$\times \int_{-\infty}^{t'} dt'' \, W(\mathbf{K}, t''). \tag{7}$$

Inserting Eq. (7) in the second of Eqs. (6) and keeping terms up to second order yields

$$\rho(\mathbf{K}, t) \approx \rho_0(\mathbf{K}, t) + \rho_1(\mathbf{K}, t) + \rho_2(\mathbf{K}, t), \tag{8}$$

where the zero-order term represents the generalization of the adiabatic following solution from atomic systems to solids,

$$\rho_0(\mathbf{K}, t) = X_0^+(\mathbf{K}, t)\rho_i(\mathbf{K})X_0(\mathbf{K}, t),$$

$$X_0(\mathbf{K}, t) = e^{i\int_{-\infty}^t d\tau \widetilde{H}(\mathbf{K}_\tau)}V^+(\mathbf{K}_t), \qquad (9)$$

where $\rho_i(\mathbf{K}) = \rho(\mathbf{K}, t = -\infty)$. Two-level adiabatic following models are tailored to perturbative NLO in atomic systems which are dominated by virtual processes [38]. We are interested in nonperturbative dynamics, where real transitions need to be accounted for as well. As such, the inclusion of higher-order Dyson terms is essential. The first- and second-order contributions are

$$\rho_1(\mathbf{K}, t) = X_1^+(\mathbf{K}, t)\rho_i(\mathbf{K})X_0(\mathbf{K}, t) + \text{H.c.}, \qquad (10)$$

$$\rho_2(\mathbf{K}, t) = \tfrac{1}{2}X_1^+(\mathbf{K}, t)\rho_i(\mathbf{K})X_1(\mathbf{K}, t)$$
$$+ X_2^+(\mathbf{K}, t)\rho_i(\mathbf{K})X_0(\mathbf{K}, t) + \text{H.c.}, \qquad (11)$$

where H.c. stands for Hermitian conjugate, and

$$X_1(\mathbf{K}, t) = \int_{-\infty}^t dt' W^+(\mathbf{K}, t')X_0(\mathbf{K}, t),$$

$$X_2(\mathbf{K}, t) = \int_{-\infty}^t dt' W^+(\mathbf{K}, t') \int_{-\infty}^{t'} dt'' W^+(\mathbf{K}, t'') X_0(\mathbf{K}, t). \qquad (12)$$

Inserting Eqs. (3), (4), (12), and the third equation of (6) into Eqs. (9)–(11) yields

$$\rho_0(\mathbf{K}, t) = \frac{1}{2}\begin{bmatrix} \frac{\lambda-\varepsilon}{\lambda} & -\frac{\Omega}{\lambda} \\ -\frac{\Omega}{\lambda} & \frac{\lambda+\varepsilon}{\lambda} \end{bmatrix}_{\mathbf{K}_t}, \qquad (13a)$$

$$\rho_1(\mathbf{K}, t) = \begin{bmatrix} \frac{\Omega}{\lambda}Re[u] & -\frac{\varepsilon}{\lambda}Re[u] - i\text{Im}[u] \\ -\frac{\varepsilon}{\lambda}Re[u] + i\text{Im}[u] & -\frac{\Omega}{\lambda}Re[u] \end{bmatrix}_{\mathbf{K}_t}, \qquad (13b)$$

$$\rho_2(\mathbf{K}, t) = \begin{bmatrix} \frac{\varepsilon}{\lambda}|u|^2 & \frac{\Omega}{\lambda}|u|^2 \\ \frac{\Omega}{\lambda}|u|^2 & -\frac{\varepsilon}{\lambda}|u|^2 \end{bmatrix}_{\mathbf{K}_t}, \qquad (13c)$$

with

$$u(\mathbf{K}, t) = -\frac{1}{2}\int_{-\infty}^t dt' \left[-\frac{\Omega(\dot{\varepsilon}\lambda - \varepsilon\dot{\lambda})}{\lambda^2(\lambda + \varepsilon)} + \frac{d}{dt'}\left(\frac{\Omega}{\lambda}\right) \right]_{\mathbf{K}_{t'}}$$
$$\times e^{-i\int_{t'}^t \lambda(\mathbf{K}_\tau)d\tau}, \qquad (14)$$

where the dot denotes the time derivative. The first term in the square bracket of Eq. (14) is of $O[(|\Omega|/\varepsilon)^3]$ and can be neglected for $|\Omega|^2/\varepsilon^2 \lesssim 1$. The integral in Eq. (14) can then be reworked by using integration by parts into

$$u(\mathbf{K}, t) = -\frac{\Omega}{2\lambda} + \mathfrak{u}(\mathbf{K}, \mathfrak{t}), \qquad (15)$$

with

$$\mathfrak{u}(\mathbf{K}, t) = \frac{i}{2}\int_{-\infty}^t dt' \Omega e^{-i\int_{t'}^t \lambda(\mathbf{K}_\tau)d\tau}. \qquad (16)$$

Next, the nonintegral parts from u in ρ_1 and ρ_2 in Eq. (15) are pulled into ρ_0. Further, terms of order $\mathfrak{u}$ and $|\mathfrak{u}|^2$ are rearranged and collected in ρ_1 and ρ_2, respectively. The resulting

density matrix is $\rho = \sum_{j=0}^2 \overline{\rho}_j$, where $\overline{\rho}_0$ and $\overline{\rho}_1$, $\overline{\rho}_2$ contain nonintegral and integral parts, respectively,

$$\overline{\rho}_0(\mathbf{K}, t) = \frac{1}{2}\begin{bmatrix} \frac{\varepsilon(\varepsilon-\lambda)}{\lambda^2} & -\frac{\Omega(\lambda-\varepsilon)}{\lambda^2} \\ -\frac{\Omega(\lambda-\varepsilon)}{\lambda^2} & 2 - \frac{\varepsilon(\varepsilon-\lambda)}{\lambda^2} \end{bmatrix}_{\mathbf{K}_t}, \qquad (17a)$$

$$\overline{\rho}_1(\mathbf{K}, t) = \begin{bmatrix} \frac{\Omega}{\lambda}Re[\mathfrak{u}] & \frac{\lambda-\varepsilon}{\lambda}Re[\mathfrak{u}] - \mathfrak{u} \\ \frac{\lambda-\varepsilon}{\lambda}Re[\mathfrak{u}] - \mathfrak{u}^* & -\frac{\Omega}{\lambda}Re[\mathfrak{u}] \end{bmatrix}_{\mathbf{K}_t}, \qquad (17b)$$

$$\overline{\rho}_2(\mathbf{K}, t) = \begin{bmatrix} \frac{\varepsilon}{\lambda}|\mathfrak{u}|^2 & \frac{\Omega}{\lambda}|\mathfrak{u}|^2 \\ \frac{\Omega}{\lambda}|\mathfrak{u}|^2 & -\frac{\varepsilon}{\lambda}|\mathfrak{u}|^2 \end{bmatrix}_{\mathbf{K}_t}. \qquad (17c)$$

It can be immediately verified from Eqs. (17) that the trace $\text{Tr}(\rho) = 1$ and that ρ is Hermitian. Finally, in the limit of intense laser fields, the dynamics is dominated by the exponent in $\mathfrak{u}$. As a result, preexponential factors of order $(|\Omega|/\varepsilon)$ and higher are of secondary significance and are neglected. This results in

$$\rho(\mathbf{K}, t) \approx \begin{bmatrix} 0 & 0 \\ 0 & 1 \end{bmatrix} + \begin{bmatrix} 0 & -\mathfrak{u} \\ -\mathfrak{u}^* & 0 \end{bmatrix}_{\mathbf{K}_t}$$
$$+ \begin{bmatrix} |\mathfrak{u}|^2 & 0 \\ 0 & -|\mathfrak{u}|^2 \end{bmatrix}_{\mathbf{K}_t}, \quad \text{with}$$

$$u(\mathbf{K}, t) = \frac{i}{2}\int_{-\infty}^t dt' \Omega(\mathbf{K}_{t'})e^{-i\int_{t'}^t \lambda(\mathbf{K}_\tau)d\tau}. \qquad (18)$$

HHG is determined by the absolute square of the Fourier transform (FT) of the expectation value of the current, $|\text{FT}\{\langle \mathbf{j} \rangle(t)\}|^2$; the current expectation value is given by $\langle \mathbf{j} \rangle(\mathbf{K}, t) = \int_{\text{BZ}} d^3K \, \text{Tr}[\rho(\mathbf{K}, t)\mathbf{j}(\mathbf{K}_t)]$.

The current operator is represented by $\mathbf{j}_{jl} = -i\langle j|\nabla|l\rangle$, with $|j\rangle, |l\rangle = |c\rangle(\mathbf{K}_t), |v\rangle(\mathbf{K}_t)$. Here, the diagonal elements $\mathbf{j}_{jj} = \nabla_{\mathbf{K}}E_j = \mathbf{v}_j(\mathbf{K})$ represent the band velocities and the band-gap velocity is defined as $\mathbf{v}(\mathbf{K}) = \mathbf{v}_c(\mathbf{K}) - \mathbf{v}_v(\mathbf{K})$. The off-diagonal terms $\mathbf{j}_{jl}\rho_{lj} = (d/dt)\mathbf{d}_{jl}(\mathbf{K}_t)\rho_{lj}(\mathbf{K}, t)$ are expressed in terms of the interband dipole moment $\mathbf{d}_{jl}$.

The current expectation value can be decomposed into contributions coming from the various density matrix expansion orders, $\langle \mathbf{j} \rangle = \sum_{j=0}^2 \langle \mathbf{j}_j \rangle$, where $\langle \mathbf{j}_j \rangle = \int_{\text{BZ}} d^3K \, \text{Tr}[\overline{\rho}_j(\mathbf{K}, t)\mathbf{j}(\mathbf{K}_t)]$. We only get HHG contributions from $\langle \mathbf{j}_1 \rangle$ and $\langle \mathbf{j}_2 \rangle$. Replacing $\langle \mathbf{j}_1 \rangle \to \langle \mathbf{j}_{er} \rangle$ and $\langle \mathbf{j}_2 \rangle \to \langle \mathbf{j}_{ra} \rangle$, we obtain interband and intraband currents,

$$\langle \mathbf{j}_{er} \rangle \approx -\frac{d}{dt}\int_{\text{BZ}} d^3K \, \mathbf{d}(\mathbf{K}_t)\mathfrak{u}(\mathbf{K}, \mathfrak{t}) + \text{c.c.}, \qquad (19a)$$

$$\langle \mathbf{j}_{ra} \rangle \approx \int_{\text{BZ}} d^3K \mathbf{v}(\mathbf{K}_t)n_c(\mathbf{K}, t). \qquad (19b)$$

Here, $n_c(\mathbf{K}, t) = |\mathfrak{u}(\mathbf{K}, \mathfrak{t})|^2$ and $n_c(t) = \int_{\text{BZ}} d^3K n_c(\mathbf{K}, t)$ is the conduction band population. In the limit of small Rabi frequency, $\lambda \to \varepsilon$ in the exponent of Eq. (18), Eqs. (19) go over into the FVB solution [32,41]. The main difference between the SFAF and FVB solutions is the dynamic Stark shift.

The density matrix in Eq. (18) fulfills $\rho = \rho^2$ to order $O(|\mathfrak{u}|^2)$, which is consistent with the order of the Dyson expansion. As such, it is reasonable to expect that it will reproduce strong-field dynamics up to the damage threshold of materials which is in the percent range of conduction band excitation. By comparison, the FVB approximation violates
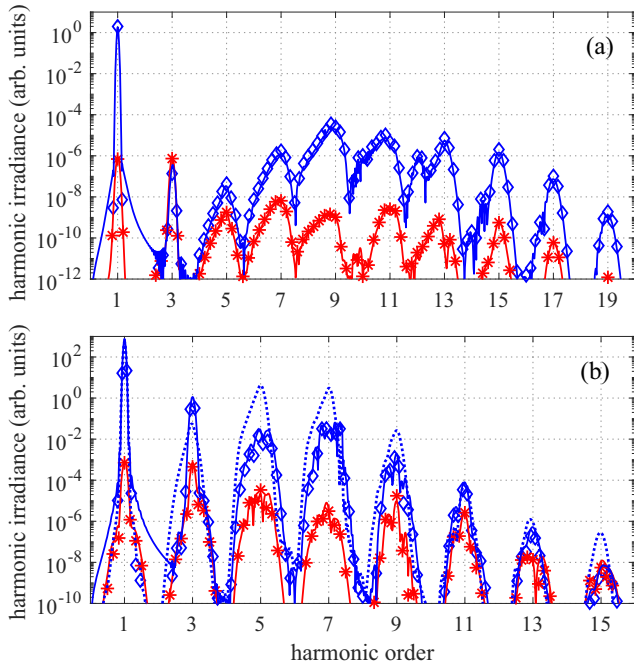
FIG. 2. (a),(b) Interband (blue full line) and intraband (full red line) HHG as obtained from the numerical solution of Eq. (1) are compared to interband (blue diamond) and intraband (red asterisk) HHG from SFAF Eqs. (19). The dotted line in (b) represents the FVB solution ($\lambda \to \varepsilon$) in Eq. (18). (a) Model semiconductor: $E_g = 0.129$, $\Delta_1 = 0.17$, $d_0 = 3.64$, $a = 5.3$; mid-ir laser: $F_0 = 0.002$ (1.2×10^{11} W/cm^2), $\omega_0 = 0.015$ (3.04 μm), $\tau_0 = 6T_0$. (b) Model dielectric: $E_g = 0.32$, $\Delta_1 = 0.06$, $\Delta_2 = -0.0035$, $\Delta_3 = -0.001$, $\Delta_4 = -0.0007$, $d_0 = 6.5$, and $a = 9.45$; near-ir laser: $F_0 = 0.012$ (4.3×10^{12} W/cm^2), $\omega_0 = 0.06$ (0.76 μm), $\tau_0 = 6T_0$.

population conservation and it is not clear whether it is accurate at all. If anything, it is expected to hold only for much smaller conduction band populations than the SFAF approach. This is explored next.

The validity of Eqs. (19) is verified by using a two-band, 1D model solid driven by a laser pulse $F(t) = F_0 \exp[-(t/\tau_0)^2] \sin(\omega_0 t)$. Here, F_0 is the peak electric field strength, ω_0 is the laser frequency (related to the laser period T_0 as $\omega_0 = 2\pi/T_0$), and τ_0 is the Gaussian half width. The band gap is given by $\varepsilon(K) = E_g + \sum_{j=1}^{n} \Delta_n[1 - \cos(nKa)]$, where a is the length of the atomic unit cell, E_g is the minimum band gap, and the half width of the band gap is mainly determined by Δ_1. The dipole moment in the $\mathbf{K} \cdot \mathbf{p}$ approximation is given by $d = d_0 \varepsilon(K = 0)/\varepsilon(K)$ for inversion symmetric materials [44]. Here, the gauge freedom of the Bloch functions has been used to chose the dipole moment to be real. We investigate two model systems representative of mid-ir semiconductor and near-ir dielectric experiments with $\Delta_1/\omega_0 \gg 1$, ~ 1, respectively. For parameters, see Fig. 2.

In Fig. 2, interband HHG (blue line) and intraband HHG (red line), as determined by a numerical solution of Eq. (1) for the model semiconductor Fig. 2(a) and dielectric [Fig. 2(b)], are compared to the harmonic spectra obtained from the currents given by Eqs. (19a) (blue diamonds) and (19b) (red asterisks). The blue dotted line in Fig. 2(b) represents FVB interband HHG. It is not shown in Fig. 2(a), as it overlaps

with the exact numerical solution. Interband HHG is dominant over the whole spectrum in Fig. 2(a). By contrast, there is a difference of up to two orders between the SFAF and FVB results for interband HHG; FVB intraband HHG is not shown, but displays similar disagreement. The greater importance of the dynamic Stark effect in dielectrics can be attributed to larger dipole moments and to higher applicable intensities due to higher damage thresholds and ultrashort laser pulses [3]. Finally, for higher harmonics, $N \geqslant 15$, the spectral intensities of inter- and intraband contributions become comparable in Fig. 2(b); see, also, Fig. 5.

III. SEPARATION OF REAL AND VIRTUAL DYNAMICS

Based on the SFAF given by Eqs. (19), a diagnostic method is developed to isolate resonant and nonresonant contributions to HHG. This is done by first splitting Eq. (18) into a probability amplitude of ionization, $\mathfrak{v}$, and into an exponent that is responsible for interband HHG,

$$u(\mathbf{K}, t) = e^{-i\int_{-\infty}^{t} d\tau \lambda(\mathbf{K}_\tau)} \mathfrak{v}(\mathbf{K}, t),$$

$$\mathfrak{v}(\mathbf{K}, t) = \frac{i}{2} \int_{-\infty}^{t} dt' \Omega(\mathbf{K}_{t'}) e^{i\int_{-\infty}^{t'} \lambda(\mathbf{K}_\tau) d\tau}. \qquad (20)$$

Then, $\mathfrak{v} = \mathfrak{v}_r + \mathfrak{v}_{nr}$ and, consequently, $\mathfrak{u} = \mathfrak{u}_r + \mathfrak{u}_{nr}$ are split into resonant and nonresonant parts based on the following argument. Whereas resonant transitions are expected to exhibit a steady increase of n_c over time, nonresonant transitions are oscillatory and all of the population returns to the valence band after the laser pulse. Mathematically, this translates into the resonant filter $G_r(\omega) = 1$ for $-\omega_0/2 \leqslant \omega \leqslant \omega_0/2$ and $G_r(\omega) = 0$ elsewhere; the nonresonant filter is $G_{nr}(\omega) = 1 - G_r(\omega)$. Therefore, the resonant (nonsinusoidal) and nonresonant (sinusoidal) transition probability amplitudes are given by

$$\mathfrak{v}_i(\mathbf{K}, t) = \text{FT}^{-1}[G_i(\omega)\tilde{\mathfrak{v}}(\mathbf{K}, \omega)], \qquad (21)$$

for $i = r, nr$, respectively. Here, FT^{-1} represents the inversion Fourier transform and $\tilde{\mathfrak{v}}$ is the Fourier transform of $\mathfrak{v}$. To separate the intraband current, $n_c = |\mathfrak{v}|^2 = n_c^r + n_c^{nr}$ also needs to be split with $n_c^i(t) = \int_{\overline{\text{BZ}}} d^3K n_c^i(\mathbf{K}, t)$ ($i = r, nr$),

$$n_c^r(\mathbf{K}, t) = |\mathfrak{v}_r(\mathbf{K}, t)|^2, \qquad (22)$$

$$n_c^{nr}(\mathbf{K}, t) = |\mathfrak{v}_{nr}(\mathbf{K}, t)|^2 + [\mathfrak{v}_{nr}(\mathbf{K}, t)\mathfrak{v}_r^*(\mathbf{K}, t) + \text{c.c.}]. \qquad (23)$$

The various processes contained in the transition probability amplitude $\mathfrak{v}$ are pictured in the schematic in Fig. 1(a). Real (resonant) transitions require energy conservation of the combined system of electron-hole pair and driving laser. As such, for a given number of photons, real transitions must occur at sharp K values at which the band gap (black line) and absorbed photon energy are the same (full circles); as a result, a resonant transition occurs when the exponent in $\mathfrak{v}$ becomes zero, resulting in a steady growth of the conduction band probability amplitude. For a finite pulse, a band of photon energies exists which widens the range of allowed resonant channels about the sharp K values (shaded area). This explains the choice of G_r above. The population from real transitions remains after the laser pulse. Virtual transitions (empty circles) reflect the distortion of the valence band ground state by the
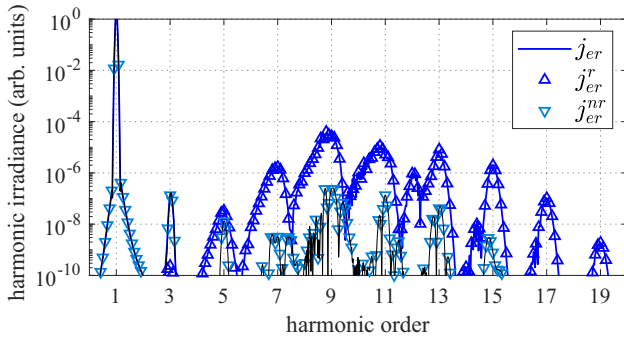
FIG. 3. Model semiconductor with the same parameters as in Fig. 2(a). HHG from j_{er} (full blue line), j_{er}^r (blue triangles up), and j_{er}^{nr} (blue triangles down, different shade of blue for visibility; thin black line is a guide to the eye) are compared. Symbols are plotted with lower resolution.

laser; the exponential in $\mathfrak{v}$ is rapidly oscillating and integrates to zero. This results in a temporary, oscillating population of conduction band states which disappears after the laser pulse.

The splitting procedure in Eq. (20) can also be rationalized mathematically. In the continuous-wave (cw) limit, a Fourier series expansion of the integrand of $\mathfrak{v}$ yields $\lim_{t\to\infty} \mathfrak{v} = \sum_n \int_0^\infty dt' c_n e^{i(\lambda_0(\mathbf{K}) + n\omega_0)t'} = \sum_n c_n(\mathbf{K})\{\pi\delta[\lambda_0(\mathbf{K}) + n\omega_0] + iP[1/(\lambda_0(\mathbf{K}) + n\omega_0)]\} = \mathfrak{v}_r + \mathfrak{v}_{nr}$ with the nonsinusoidal term $\lambda_0(\mathbf{K})$ a field dressed bandwidth [black line in Fig. 1(a)], and c_n Fourier coefficients. The δ function and principal value P represent resonant (r, full circle) and nonresonant (nr, empty circle) transitions for each K value in Fig. 1(a), respectively. As a result of the Fourier series expansion, each term contains the sum over all possible channels resulting in the absorption of n photons; see Fig. 1(b). In going from cw to finite pulses, the black line in Fig. 1(a) morphs into the gray shaded area. We would like to emphasize that separating real from virtual absorption channels would not be possible without having the closed-form expression for the transition probability amplitude $\mathfrak{v}$, given by Eq. (20). The above discussion shows why real and virtual channels are difficult to disentangle in intense laser fields; many channels consisting of photons with varying energies contribute to each real and virtual transition.

With the above definitions, the resonant and nonresonant interband and intraband currents are

$$\langle \mathbf{j}_{er}^i \rangle \approx -\frac{d}{dt} \int_{\overline{BZ}} d^3K \, \mathbf{d}(\mathbf{K}_t) \, \mathfrak{u}_i(\mathbf{K}, \mathfrak{t}) + \text{c.c.}, \quad (24)$$

$$\langle \mathbf{j}_{ra}^i \rangle \approx \int_{\overline{BZ}} d^3K \, \mathbf{v}(\mathbf{K}_t) n_c^i(\mathbf{K}, t) \quad (i = r, nr). \quad (25)$$

Now, Eqs. (20)–(25) are applied to the model systems of Fig. 2 to separate resonant from nonresonant HHG. The markers in Figs. 2–5 were chosen to reflect the relation between HHG currents. Interband HHG: j_{er} (diamonds) = j_{er}^r (triangle up) + j_{er}^{nr} (triangle down); triangle up and down combine to a diamond. Intraband HHG: j_{ra} (asterisk) = j_{ra}^r (cross) + j_{ra}^{nr} (plus); plus and cross combine to an asterisk. For n_c^i, the same symbols are used as for j_{ra}^i ($i = r, nr$). From here on, all results shown are from SFAF calculations, as
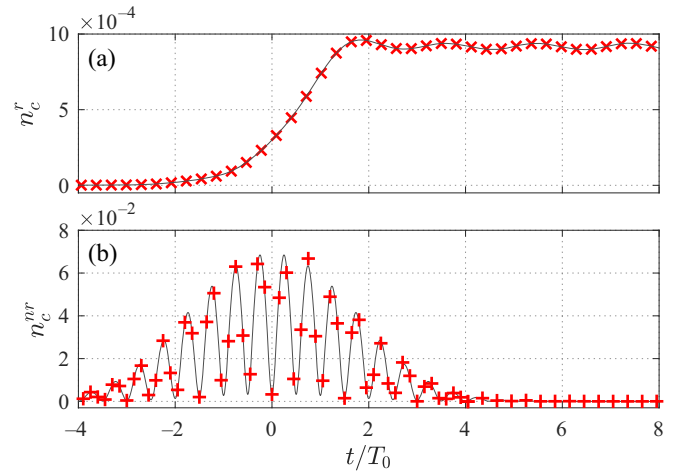

FIG. 4. (a),(b) Conduction population time evolution for the model dielectric; parameters are the same as in Fig. 2(b), except for $\tau_0 = 3T_0$ and $F_0 = 0.02$. (a) n_c^r [Eq. (22), red cross] and (b) n_c^{nr} [Eq. (23), red plus]; thin black lines are guides to the eye.

they are practically indistinguishable from the exact numerical results.

In Fig. 3, the interband harmonic spectrum from Fig. 2(a) is split into resonant and nonresonant contributions. HHG from the full interband current (19a) (blue full line), and from resonant (blue triangles up) and nonresonant interband currents (blue triangles down) in Eq. (24), are compared. HHG for $N = 1, 3$ is nonresonant and turns resonant for $N > 5$; the first above band-gap harmonic is $N = 9$. The above minimum

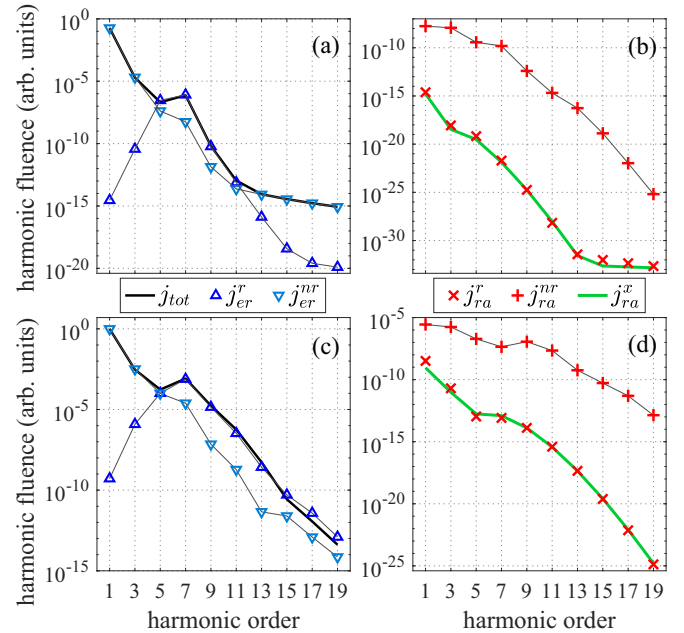

FIG. 5. Same parameters as in Fig. 4, except for (a),(b) $F_0 = 0.005$ and (c),(d) $F_0 = 0.012$. Thin gray lines serve as a guide to the eye. (a),(c) HHG from interband currents j_{er}^r (blue triangles up) and j_{er}^{nr} (blue triangles down), HHG from total current (black full line). (b),(d) HHG from intraband currents j_{ra}^r (red crosses), j_{ra}^{nr} (red pluses), j_{ra}^x (green full lines); see text.

band-gap harmonics are resonant, in agreement with previous theoretical [32–35,37] and experimental [25,27,45] work.

In the model dielectric of Fig. 2(b), intraband currents j_{ra}^i and thereby populations n_c^i ($i = r, nr$) become relevant; n_c^r (red crosses) and n_c^{nr} (red plus) are plotted in Figs. 4(a) and 4(b), respectively. The parameters are the same as in Fig. 2(b), except for $F_0 = 0.02$ and a shorter pulse duration $\tau = 3T_0$ usually used in high-intensity experiments. As required, the resonant contribution keeps steadily growing and reaches a constant value after the laser pulse. Usually, tunnel ionization calculations display a subcycle, steplike increase arising from the exponential subcycle field dependence. Our formalism counts the steplike increase as part of the nonresonant oscillations about the (cycle-averaged) resonant ionization curve displayed in Fig. 4(b). The nonresonant, virtual contribution n_c^{nr} is oscillatory and goes to zero after the pulse.

HHG in the model dielectric is plotted in Fig. 5 for $F_0 = 0.005$ [Figs. 5(a) and 5(b)] and for $F_0 = 0.012$ [Figs. 5(c) and 5(d)]; the remaining parameters are as in Fig. 4. Figures 5(a), 5(c) and Figs. 5(b), 5(d) show interband and intraband currents, respectively. For clarity, we plot the harmonic fluence by integrating harmonic signals over the frequency interval $|\omega - N\omega_0| < (\omega_0/2)$. The first above minimum band-gap harmonic is $N = 7$. In Figs. 5(a) and 5(b), the total harmonic signal (black full line) is composed of a mixture of j_{er}^r (blue triangles up) and j_{er}^{nr} (blue triangles down); intraband currents [Fig. 5(b)] are negligible; the resonant intraband current (red crosses) is weakest. For higher F_0 [Figs. 5(c) and 5(d)], j_{er}^r (blue triangles up) is dominant for $N > 5$ and accounts for most of the total harmonic signal (full black line) in Fig. 5(c). For $N \geqslant 11$, j_{ra}^{nr} (red plus) becomes comparable to j_{er}^r, which results in interference and a suppression of the total HHG signal; compare triangles pointing up with black line. Again, j_{ra}^r (red crosses) is weakest. This explains why HHG from j_{ra}^r could not be observed in numerical analysis of the semiconductor Bloch equations [3,4]. Finally, this presents direct identification of the relevance of virtual HHG channels. Their greater importance in near-ir dielectric experiments can be attributed to the dynamic Stark effect, which increases the effective minimum band gap and thus weakens resonant transitions [41].

Beyond that, another relevant finding ensues from comparison to experiments. Near-ir dielectric HHG [3,5,9] can be explained quite well by a simple model (Bloch oscillation) current,

$$j_{ra}^x = c|\text{FT}[v(A(t))]|^2, \tag{26}$$

where c is a constant. It can be obtained from Eq. (25) by assuming that the conduction band population is δ-function-like around $K = 0$. It is represented by the green line in Figs. 4(b) and 4(d), which has been matched to j_{ra}^r by determining c at harmonic $N = 9$. The constant is found to be of the order of $n_c^2(t \to \infty)$. The agreement between j_{ra}^r and j_{ra}^x is excellent in both cases. Note that the (cycle-averaged) resonant ionization rate does not contain harmonic terms so that resonant intraband HHG comes solely from the band velocity.

The negligible contribution of j_{ra}^r to the total current in Fig. 5 conflicts with the fact that j_{ra}^x was successfully used to describe near-ir experiments in dielectrics [3] and below band-gap harmonics in some semiconductors [6]. The apparent contradiction indicates that important physics is missing in the semiconductor Bloch analysis. An important missing element is dephasing, be it through propagation [46–48] or through microscopic scattering processes. We would like to note that ultrathin samples have been used in the above experiments [3] to minimize the influence of propagation effects. Dephasing can strongly affect the oscillatory parts of $e^{i\int_{t'}^t \lambda d\tau}$ in Eq. (18), thus suppressing HHG. The presence of dephasing should favor j_{ra}^r, as it is the only nonoscillatory current that changes on the timescale of the laser envelope. Dephasing in the relaxation time approximation is a crude approach. It introduces additional strongly dephasing time-dependent transitions to the conduction band [49], which can exceed regular transition channels. This makes its use questionable. Further, in previous work, it could not explain the dominance of j_{ra}^r, except for unreasonably short dephasing times [3]. Therefore, more refined dephasing models will need to be developed by coupling to the many-body reservoir of condensed matter, for example, via a harmonic-oscillator heat bath.

IV. CONCLUSION

We have developed the strong-field adiabatic following (SFAF) approach that yields a closed-form solution for modeling strong-field processes in solids. Based on that, a diagnostic tool has been derived that allows the separation of real from virtual nonlinear processes. Our approach has been tested and studied for 1D, two-band model semiconductors and dielectrics. The SFAF equations can be evaluated very efficiently and lend themselves ideally to coupling with Maxwell's equations for studying macroscopic HHG effects.

The SFAF approach can be extended to more than two bands. For systems with a limited number of dipole-active bands ($n \leqslant 4$), by-hand diagonalization of the Hamiltonian is still possible; for larger n's, algebraic software packages will have to be used. Also, we have performed preliminary 3D studies with linearly polarized laser fields which show a similarly good agreement between closed-form and exact solutions. Studies of more realistic systems in dependence on elliptic polarization and/or varying linear polarization direction are subject to future research.

In terms of physics, our study has confirmed the dominance of the interband recollision model in mid-ir semiconductor experiments. In near-ir dielectrics, due to stronger dipole moments and higher damage thresholds, the dynamic Stark shift becomes more pronounced and suppresses optical field ionization. As a result, real and virtual HHG channels can become comparable.

HHG in near-ir-driven dielectrics can be explained in terms of the simple classical model derived from the intraband current. This is starkly different from the interband recollision mechanism found in mid-ir semiconductors. The physical mechanisms responsible for this difference have remained a mystery to date. Neither numerical *ab initio* calculations nor simple models have been able to explain it.

We have identified the resonant intraband current to be the weakest of all contributions, in contradiction to experiments. Interband HHG depends on the accumulation of a

quantum phase during the laser-driven evolution of electron-hole pairs. By contrast, intraband HHG depends only on the band velocity and not on phase terms. As such, one possibility to explain the apparent contradiction between theory and experiment is that dephasing suppresses the other HHG channels and makes intraband HHG dominant. This reveals evidence that collisional many-body processes going beyond one-electron-hole and mean-field approaches might be important. The method developed here lays the necessary theoretical foundation to further pursue the above ideas.

[1] S. Ghimire, P. Agostini, D. A. Reis, S. Ghimire, L. F. DiMauro, and E. Sistrunk, Observation of high-order harmonic generation in a bulk crystal, Nat. Phys. **7**, 138 (2011).

[2] G. Vampa, T. J. Hammond, N. Thiré, B. E. Schmidt, F. Légaré, C. R. McDonald, T. Brabec, D. D. Klug, and P. B. Corkum, All-Optical Reconstruction of Crystal Band Structure, Phys. Rev. Lett. **115**, 193603 (2015).

[3] T. T. Luu, M. Garg, S. Yu Kruchinin, A. Moulet, M. Th. Hassan, and E. Goulielmakis, Extreme ultraviolet high-harmonic spectroscopy of solids, Nature (London) **521**, 498 (2015).

[4] M. Garg, M. Zhan, T. T. Luu, H. Lakhotia, T. Klostermann, A. Guggenmos, and E. Goulielmakis, Multi-petahertz electronic metrology, Nature (London) **538**, 359 (2016).

[5] M. Garg, H. Y. Kim, and E. Goulielmakis, Ultimate waveform reproducibility of extreme-ultraviolet pulses by high-harmonic generation in quartz, Nat. Photon. **12**, 291 (2018).

[6] A. A. Lanin, E. A. Stepanov, A. B. Fedotov, and A. M. Zheltikov, Mapping the electron band structure by intra-band high-harmonic generation in solids, Optica **4**, 516 (2017).

[7] H. Liu, Y. Li, Y. S. You, S. Ghimire, T. F. Heinz, and D. A. Reis, High-harmonic generation from an atomically thin semiconductor, Nat. Phys. **13**, 262 (2017).

[8] T. T. Luu and H. J. Wörner, Measurement of the Berry curvature of solids using high-harmonic spectroscopy, Nat. Commun. **9**, 916 (2018).

[9] H. Lakhotia, H. Y. Kim, M. Zhan, S. Hu, S. Meng, and E. Goulielmakis, Laser picoscopy of valence electrons in solids, Nature (London) **583**, 55 (2020).

[10] S. Jiang, J. Chen, H. Wei, C. Yu, R. Lu, and C. D. Lin, Role of the Transition Dipole Amplitude and Phase on the Generation of Odd and Even High-Order Harmonics in Crystals, Phys. Rev. Lett. **120**, 253201 (2018).

[11] D. Bauer and K. K. Hansen, High-Harmonic Generation in Solids with and without Topological Edge States, Phys. Rev. Lett. **120**, 177401 (2018).

[12] R. E. F. Silva, Á. Jiménez-Galán, B. Amorim, O. Smirnova, and M. Ivanov, Topological strong-field physics on sub-laser-cycle timescale, Nat. Photon. **13**, 849 (2019).

[13] Á. Jiménez-Galán, R. E. F. Silva, O. Smirnova, and M. Ivanov, Lightwave control of topological properties in 2D materials for sub-cycle and non-resonant valley manipulation, Nat. Photon. **14**, 728 (2020).

[14] D. Baykusheva, A. Chacón, D. Kim, D. E. Kim, D. A. Reis, and S. Ghimire, Strong-field physics in three-dimensional topological insulators, Phys. Rev. A **103**, 023101 (2021).

[15] A. Chacón, D. Kim, W. Zhu, S. P. Kelly, A. Dauphin, E. Pisanty, A. S. Maxwell, A. Picón, M. F. Ciappina, D. E. Kim, C. Ticknor, A. Saxena, and M. Lewenstein, Circular dichroism in higher-order harmonic generation: Heralding topological phases and transitions in Chern insulators, Phys. Rev. B **102**, 134115 (2020).

[16] C. P. Schmid, L. Weigl, P. Grössing, V. Junk, C. Gorini, S. Schlauderer, S. Ito, M. Meierhofer, N. Hofmann, D. Afanasiev, J. Crewse, K. A. Kokh, O. E. Tereshchenko, J. Güdde, F. Evers, J. Wilhelm, K. Richter, U. Höfer, and R. Huber, Tunable noninteger high-harmonic generation in a topological insulator, Nature (London) **593**, 385 (2021).

[17] D. Baykusheva, A. Chacón, J. Lu, T. P. Bailey, J. A. Sobota, H. Soifer, P. S. Kirchmann, C. Rotundu, C. Uher, T. F. Heinz, D. A. Reis, and S. Ghimire, All-optical probe of three-dimensional topological insulators based on high-harmonic generation by circularly polarized laser fields, Nano Lett. **21**, 8970 (2021).

[18] R. E. F. Silva, I. V. Blinov, A. N. Rubtsov, O. Smirnova, and M. Ivanov, High-harmonic spectroscopy of ultrafast many-body dynamics in strongly correlated systems, Nat. Photon. **12**, 266 (2018).

[19] Y. Murakami, M. Eckstein, and P. Werner, High-Harmonic Generation in Mott Insulators, Phys. Rev. Lett. **121**, 057405 (2018).

[20] Y. Murakami, S. Takayoshi, A. Koga, and P. Werner, High-harmonic generation in one-dimensional Mott insulators, Phys. Rev. B **103**, 035110 (2021).

[21] K. Uchida, G. Mattoni, S. Yonezawa, F. Nakamura, Y. Maeno, and K. Tanaka, High-Order Harmonic Generation and Its Unconventional Scaling Law in the Mott-Insulating Ca_2RuO_4, Phys. Rev. Lett. **128**, 127401 (2022).

[22] O. Schubert, M. Hohenleutner, F. Langer, B. Urbanek, C. Lange, U. Huttner, D. Golde, T. Meier, M. Kira, S. W. Koch, and R. Huber, Sub-cycle control of terahertz high-harmonic generation by dynamical Bloch oscillations, Nat. Photon. **8**, 119 (2014).

[23] F. Langer, M. Hohenleutner, C. P. Schmid, C. Poellmann, P. Nagler, T. Korn, C. Schüller, M. S. Sherwin, U. Huttner, J. T. Steiner, S. W. Koch, M. Kira, and R. Huber, Lightwave-driven quasiparticle collisions on a subcycle timescale, Nature (London) **533**, 225 (2016).

[24] U. Huttner, M. Kira, and S. W. Koch, Ultrahigh off-resonant field effects in semiconductors, Laser Photon. Rev. **11**, 1700049 (2017).

[25] G. Vampa, T. J. Hammond, N. Thiré, B. E. Schmidt, F. Légaré, C. R. McDonald, T. Brabec, and P. B. Corkum, Linking high harmonics from gases and solids, Nature (London) **522**, 462 (2015).

[26] N. Yoshikawa, K. Nagai, K. Uchida, Y. Takaguchi, S. Sasaki, Y. Miyata, and K. Tanaka, Interband resonant high-harmonic generation by valley polarized electron-hole pairs, Nat. Commun. **10**, 3709 (2019).

[27] A. J. Uzan, G. Orenstein, Á. Jiménez-Galán, C. McDonald, R. E. F. Silva, B. D. Bruner, N. D. Klimkin, V. Blanchet, T. Arusi-Parpar, M. Krüger, A. N. Rubtsov, O. Smirnova,

M. Ivanov, Y. Binghai, T. Brabec, and N. Dudovich, Attosecond spectral singularities in solid-state high-harmonic generation, Nat. Photon. **14**, 183 (2020).

[28] M. Wu, Y. You, S. Ghimire, D. A. Reis, D. A. Browne, K. J. Schafer, and M. B. Gaarde, Orientation dependence of temporal and spectral properties of high-order harmonics in solids, Phys. Rev. A **96**, 063412 (2017).

[29] D. Dimitrovski, T. G. Pedersen, and L. B. Madsen, Floquet-Bloch shifts in two-band semiconductors interacting with light, Phys. Rev. A **95**, 063420 (2017).

[30] N. Tancogne-Dejean, O. D. Mücke, F. X. Kärtner, and A. Rubio, Ellipticity dependence of high-harmonic generation in solids originating from coupled intraband and interband dynamics, Nat. Commun. **8**, 745 (2017).

[31] R. E. F. Silva, F. Martíín, and M. Ivanov, High harmonic generation in crystals using maximally localized Wannier functions, Phys. Rev. B **100**, 195201 (2019).

[32] G. Vampa, C. R. McDonald, G. Orlando, D. D. Klug, P. B. Corkum, and T. Brabec, Theoretical Analysis of High-Harmonic Generation in Solids, Phys. Rev. Lett. **113**, 073901 (2014).

[33] G. Vampa, C. R. McDonald, G. Orlando, P. B. Corkum, and T. Brabec, Semiclassical analysis of high harmonic generation in bulk crystals, Phys. Rev. B **91**, 064302 (2015).

[34] L. Li, P. Lan, X. Zhu, T. Huang, Q. Zhang, M. Lein, and P. Lu, Reciprocal-Space-Trajectory Perspective on High-Harmonic Generation in Solids, Phys. Rev. Lett. **122**, 193901 (2019).

[35] L. Yue and M. B. Gaarde, Imperfect Recollisions in High-Harmonic Generation in Solids, Phys. Rev. Lett. **124**, 153204 (2020).

[36] L. Yue and M. B. Gaarde, Introduction to theory of high-harmonic generation in solids: Tutorial, J. Opt. Soc. Am. B **39**, 535 (2022).

[37] A. M. Parks, G. Ernotte, A. Thorpe, C. R. McDonald, P. B. Corkum, M. Taucer, and T. Brabec, Wannier quasi-classical approach to high harmonic generation in semiconductors, Optica **7**, 1764 (2020).

[38] R. W. Boyd, *Nonlinear Optics*, 2nd ed. (Academic, San Diego, 2003).

[39] Y. Sanari, H. Hirori, T. Aharen, H. Tahara, Y. Shinohara, K. L. Ishikawa, T. Otobe, P. Xia, N. Ishii, J. Itatani, S. A. Sato, and Y. Kanemitsu, Role of virtual band population for high harmonic generation in solids, Phys. Rev. B **102**, 041125(R) (2020).

[40] T. Boolakee, C. Heide, A. Garzón-Ramírez, H. B. Weber, I. Franco, and P. Hommelhoff, Light-field control of real and virtual charge carriers, Nature (London) **605**, 251 (2022).

[41] C. R. McDonald, G. Vampa, P. B. Corkum, and T. Brabec, Intense-Laser Solid State Physics: Unraveling the Difference between Semiconductors and Dielectrics, Phys. Rev. Lett. **118**, 173601 (2017).

[42] C. R. McDonald, G. Vampa, P. B. Corkum, and T. Brabec, Interband Bloch oscillation mechanism for high-harmonic generation in semiconductor crystals, Phys. Rev. A **92**, 033845 (2015).

[43] J. J. Sakurai and J. Napolitano, *Modern Quantum Mechanics*, 2nd ed. (Addison-Wesley, San Francisco, 2011).

[44] H. Haug and S. W. Koch, *Quantum Theory of the Optical and Electronic Properties of Semiconductors*, 5th ed. (World Scientific, Singapore, 2009).

[45] G. Vampa, J. Lu, Y. S. You, D. R. Baykusheva, M. Wu, H. Liu, K. J. Schafer, M. B. Gaarde, D. A. Reis, and S. Ghimire, Attosecond synchronization of extreme ultraviolet high harmonics from crystals, J. Phys. B: At. Mol. Opt. Phys. **53**, 144003 (2020).

[46] I. Floss, C. Lemell, G. Wachter, V. Smejkal, S. A. Sato, X. Tong, K. Yabana, and J. Burgdörfer, *Ab initio* multiscale simulation of high-order harmonic generation in solids, Phys. Rev. A **97**, 011401(R) (2018).

[47] I. Kilen, M. Kolesik, J. Hader, J. V. Moloney, U. Huttner, M. K. Hagen, and S. W. Koch, Propagation Induced Dephasing in Semiconductor High-Harmonic Generation, Phys. Rev. Lett. **125**, 083901 (2020).

[48] P. Jürgens, P. Jürgens, B. Kruse, C. Peltz, D. Engel, A. Husakou, T. Witting, M. Ivanov, M. J. J. Vrakking, T. Fennel, and A. Mermillod-Blondin, Origin of strong-field-induced low-order harmonic generation in amorphous quartz, Nat. Phys. **16**, 1035 (2020).

[49] C. R. McDonald, A. Ben Taher, and T. Brabec, Strong field optical ionization of solids, J. Opt. **19**, 114005 (2017).